INTERNATIONAL JOURNAL OF ENERGY RESEARCH
*Int. J. Energy Res.* 2010; **34**:107–115
Published online 25 November 2009 in Wiley InterScience
(www.interscience.wiley.com). DOI: 10.1002/er.1652

# Electrochemical–thermal modeling of automotive Li-ion batteries and experimental validation using a three-electrode cell

Weifeng Fang[1], Ou Jung Kwon[2] and Chao-Yang Wang[1,2,*,†]

[1]*Department of Mechanical and Nuclear Engineering, Electrochemical Engine Center, The Pennsylvania State University, University Park, PA 16802, U.S.A.*
[2]*Department of Materials Science and Engineering, Electrochemical Engine Center, The Pennsylvania State University, University Park, PA 16802, U.S.A.*

## SUMMARY

An electrochemical–thermal-coupled model is used to predict performance of a Li-ion cell as well as its individual electrodes at various operating temperatures. The model is validated against the experimental data for constant current and pulsing conditions characteristic of hybrid electric vehicle (HEV) applications. The prediction of individual electrode potential is also compared with 3-electrode cell experimental data with good agreement. The predictive ability of the individual electrode behavior is very useful to address important issues related to electrode degradation and subzero performance of automotive Li-ion batteries. Copyright © 2009 John Wiley & Sons, Ltd.

KEY WORDS: lithium-ion battery; electrochemical modeling; hybrid-electric vehicles; three-electrode cell; transient; heat generation

## 1. INTRODUCTION

Li-ion batteries for both hybrid electric vehicles (HEVs) and plug-in HEVs will play a central role in fuel-efficient, low-emission automobiles. Salient advantages of Li-ion batteries for HEVs, as opposed to the currently used nickel-metal hydride battery, are that they offer 40–50% weight reduction and 20–30% volume reduction as well as a margin of efficiency improvement [1]. The development and implementation of Li-ion batteries in automobiles, however, require substantial diagnostic and modeling efforts in order to fully understand the fundamentals governing their performance, cycle life, safety, and cost.

In particular, electrochemical–thermal (ECT)-coupled phenomena in Li-ion batteries must be captured, as they control major technological hurdles of current interest, such as thermal runaway at high temperatures, much reduced performance at subzero temperatures, and Li plating in the anode and capacity loss under high-rate, low-temperature charging. To date, both experimental and modeling research on thermal and electrochemical characteristics are mostly limited to full Li-ion cells. For example, early models of Li-ion

*Correspondence to: Chao-Yang Wang, Department of Mechanical and Nuclear Engineering, Electrochemical Engine Center, The Pennsylvania State Univerisity, Univeristy Park, PA 16802, U.S.A.
†E-mail: cxw31@psu.edu


*Received 5 October 2009*
*Accepted 8 October 2009*

cells were developed by Newman and co-workers using porous electrode and concentrated solution theories [2–4] under isothermal and one-dimensional (1D) assumptions. Subsequently Wang and coworkers have focused on ECT-coupled modeling for Li-ion batteries, especially for automotive applications [5–9]. Model validation was performed against experimental data of full cells only.

Stringent automotive application, however, calls for detailed diagnostics and modeling of not only the full cell but also individual electrodes such that anode and cathode contributions to both performance and degradation can be separately delineated and predicted. For example, lithium deposition on the negative electrode in overcharge or low temperature situations and degradation of a Li-ion battery due to surface film formation on both electrodes all require a good understanding of individual electrode behaviors in addition to a full cell. Thus, in this work we aim to develop and experimentally validate a capability to predict performance of individual electrodes of Li-ion cells under HEV conditions that encompass a wide range of ambient temperatures. This work is an extension of our previous work on development of comprehensive Li-ion battery models for HEV design, operation, and control [5–9].

## 2. EXPERIMENTAL

Commercial 1.2 A h 18650 cells with a graphite anode and a nickel–manganese–cobalt oxide (NMC) cathode as well as the electrolyte of 1.2 M LiPF6 in EC/DMC are used in all experiments. In order to measure each electrode potential separately, a Li reference electrode is installed to form a 3-electrode cell in an argon-filled glove box where both oxygen and water levels must be maintained at less than 1 ppm. Also, a thermocouple is inserted inside the 3-electrode cell holder to monitor the average cell temperature as represented by a lump thermal model to be described shortly. The 3-electrode cell is then sealed tightly before removal from the glove box. Other details about the 3-eletrode cell assembly and temperature/potential measurements can be found in Zhang and Wang [10]. All experiments are carried out under constant ambient temperatures in a Tenney Environmental Chamber (Series 942). Before each test, a test cell is rested in the chamber for at least 2 h in order to reach thermal equilibrium, as monitored by the internal thermocouple.

## 3. MATHEMATICAL MODELING

The present model consists of a 1D electrochemical-transport model and a lumped thermal model where a spatially uniform but temporally varying cell temperature is assumed. This will be termed as ECT-coupled model in the following sections. It should be noted that uniform current distribution is assumed over the entire electrode area.

### *3.1. 1D Electrochemical model*

A typical Li-ion cell consists of a negative electrode, an electrolyte separator, and a positive electrode, as shown in Figure 1. The electrolyte, a good ionic conductor but an electronic insulator, provides a medium for Li ions to travel between the two electrodes and keeps electrons flowing in the external circuit. During charge, Li ions extract from lithiated NMC oxide particles in the positive electrode, travel through the electrolyte separator,

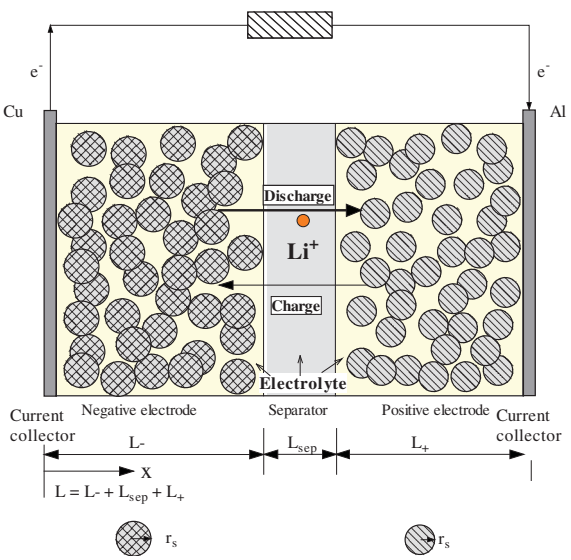


Figure 1. Schematic of 1D ($x$-direction) Li-ion cell model coupled with microscopic ($r$-direction) solid-diffusion submodel.



DOI: 10.1002/er

Table I. Governing equations of Li-ion cell model.

| Conservation equations | | | Boundary conditions |
|---|---|---|---|
| Charge, solid phase | $\frac{\partial}{\partial x}\left(\sigma^{\text{eff}}\frac{\partial}{\partial x}\phi_{\text{s}}\right)=j^{\text{Li}}$ | (1) | $-\sigma_{-}^{\text{eff}}\frac{\partial\phi_{\text{s}}}{\partial x}\Big\vert_{x=0}=\sigma_{+}^{\text{eff}}\frac{\partial\phi_{\text{s}}}{\partial x}\Big\vert_{x=L}=\frac{I}{A}$ |
| | | | $\frac{\partial\phi_{\text{s}}}{\partial x}\Big\vert_{x=L_{-}}=\frac{\partial\phi_{\text{s}}}{\partial x}\Big\vert_{x=L_{-}+L_{\text{sep}}}=0$ |
| Charge, electrolyte phase | $\frac{\partial}{\partial x}\left(\kappa^{\text{eff}}\frac{\partial}{\partial x}\phi_{\text{e}}\right)+\frac{\partial}{\partial x}\left(\kappa_{\text{D}}{}^{\text{eff}}\frac{\partial}{\partial x}\ln c_{\text{e}}\right)=-j^{\text{Li}}$ | (2) | $\frac{\partial\phi_{\text{e}}}{\partial x}\Big\vert_{x=0}=\frac{\partial\phi_{\text{e}}}{\partial x}\Big\vert_{x=L}=0$ |
| Species, electrolyte phase | $\frac{\partial(\varepsilon_{\text{e}}c_{\text{e}})}{\partial t}=\frac{\partial}{\partial x}\left(D_{\text{e}}{}^{\text{eff}}\frac{\partial}{\partial x}c_{\text{e}}\right)+\frac{1-t_{+}^{o}}{F}j^{\text{Li}}$ | (3) | $\frac{\partial c_{\text{e}}}{\partial x}\Big\vert_{x=0}=\frac{\partial c_{\text{e}}}{\partial x}\Big\vert_{x=L}=0$ |
| Species, solid phase | $\frac{\partial c_{\text{s}}}{\partial t}=\frac{D_{\text{s}}}{r^2}\frac{\partial}{\partial r}\left(r^2\frac{\partial c_{\text{s}}}{\partial r}\right)$ | (4) | $\frac{\partial c_{\text{s}}}{\partial r}\Big\vert_{r=0}=0,\ -D_{\text{s}}\frac{\partial c_{\text{s}}}{\partial r}\Big\vert_{r=R_{\text{s}}}=\frac{j^{\text{Li}}}{a_{\text{s}}F}$ |

and insert into graphite particles in the negative electrode. Simultaneously, electrons released from the positive electrode flow through an external circuit towards the negative electrode. During discharge Li ions and electrons travel in the reverse direction.

Porous electrode theory is adopted in modeling the composite electrodes consisting of active materials and the electrolyte. The solid and electrolyte phases are treated as superimposed *continua* with each phase having its own volume fraction, while the microstructural morphology of each phase is not considered. To account for tortuosity effects, the electrolyte diffusion coefficient and ionic conductivity are corrected by the Bruggeman factor, $D_{\text{e}}^{\text{eff}}=D_{\text{e}}\varepsilon_{\text{e}}^{p}$ and $\kappa^{\text{eff}}=\kappa\varepsilon_{\text{e}}^{p}$, respectively, where $p$ is the Bruggeman exponent. Similarly the electronic conductivity is corrected as $\sigma^{\text{eff}}=\sigma\varepsilon_{\text{s}}^{p}$ for each electrode. Here, $\varepsilon_{\text{e}}$ and $\varepsilon_{\text{s}}$ are the electrolyte and solid phase volume fractions, respectively.

The final governing equations of species and charge conservation are summarized in Table I. For more details about the present modeling approach, refer to the references [2,6].

Reaction rates for Li insertion and extraction reactions are generally assumed to follow the Butler–Volmer equation:

$$j^{\text{Li}}=a_{\text{s}}i_0\left[\exp\left(\frac{\alpha_{\text{a}}F}{RT}\eta-\frac{R_{\text{SEI}}}{a_{\text{s}}}j^{\text{Li}}\right)-\exp\left(-\frac{\alpha_{\text{c}}F}{RT}\eta-\frac{R_{\text{SEI}}}{a_{\text{s}}}j^{\text{Li}}\right)\right] \tag{5}$$

where $F$ is Faraday's constant, $R$ the universal gas constant, and $\alpha_{\text{a}}$ and $\alpha_{\text{c}}$ the anodic and cathodic transfer coefficients of electrode reactions, respectively. The exchange current density, $i_0$, is a function of lithium concentrations in both electrolyte and solid active materials, i.e. $i_0=k(c_{\text{e}})^{\alpha_{\text{a}}}(c_{\text{s,max}}-c_{\text{s,e}})^{\alpha_{\text{a}}}(c_{\text{s,e}})^{\alpha_{\text{c}}}$, where $c_{\text{e}}$ and $c_{\text{s}}$ are the volume-averaged lithium concentration in the electrolyte and solid phases, respectively, $c_{\text{s,e}}$ is the area-averaged solid-state lithium concentration at the electrode/electrolyte interface, and $c_{\text{s,max}}$ is the maximum concentration of lithium in the solid phase. The constant, $k$, is determined by the exchange current density under standard species concentrations. The local surface overpotential, $\eta$, is defined as the difference between the solid and liquid phase potential with respect to the open-circuit potential (OCP), $U$, or $\eta=\phi_{\text{s}}-\phi_{\text{e}}-U$. The OCP is a function of local state of charge, defined as $\text{SOC}=c_{\text{s,e}}/c_{\text{s,max}}$, and temperature. In the present work, OCP values for the negative and positive electrodes are estimated from the experimental data measured by Kwon and Wang [11], see Figure 2. $R_{\text{SEI}}$ represents the electronic resistance of the surface film layer at the negative and positive electrode.

The diffusional conductivity, $\kappa_{\text{D}}^{\text{eff}}$, is given by concentrated solution theory [3], as

$$\kappa_{\text{D}}^{\text{eff}}=\frac{2RT\kappa^{\text{eff}}}{F}(t_{+}^{0}-1)\left(1+\frac{\text{d}\ln f_{\pm}}{\text{d}\ln c_{\text{e}}}\right) \tag{6}$$

where $f_{\pm}$ is the mean molar activity coefficient of the electrolyte. The electrolyte phase ionic conductivity, $\kappa$, strongly depends on the electrolyte compositions. For the electrolyte consisting of 1.2 M LiPF6 in a 2:1 v/v mixture of ethylene carbonate (EC) and dimethyl carbonate (DMC), one



DOI: 10.1002/er

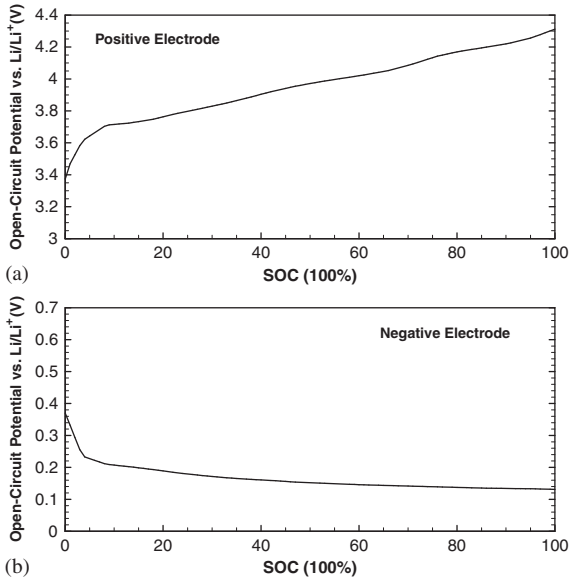


Figure 2. Measured open-circuit potentials vs Li/Li+ of: (a) positive electrode and (b) negative electrode using a three-electrode cell at 25°C.

has [4],

$$\kappa = 4.1253 \times 10^{-4} + 5.007 c_e - 4.7212 \times 10^{3} c_e^2 + 1.5094 \times 10^{6} c_e^3 - 1.6018 \times 10^{8} c_e^4 \quad (7)$$

The governing equations listed in Table I, Equations (1)–(3), describe macroscopic transport along the thickness of the cell ($x$-direction), i.e. from the negative electrode to separator and to positive electrode. In contrast, Equation (4) in Table I describes the microscopic solid-state diffusion of Li ions in active material particles ($r$-direction), as seen in Figure 1. The combined micro/macroscopic model is essential to describe Li-ion cell behaviors.

### 3.2. Lumped thermal model

The foregoing 1D electrochemical model is then coupled to a lumped thermal model which assumes that the cell temperature is spatially uniform and can be calculated by the following heat balance equation:

$$\frac{\mathrm{d}(\rho c_p T)}{\mathrm{d}t} = hA_s(T - T_\infty) + (q_r + q_j + q_c + q_e)A \quad (8)$$

Here $h$ is the coefficient of heat dissipation to the ambient, $A_s$ the cell external surface area, and $T_\infty$ the ambient temperature. The total reaction heat, $q_r$, is calculated by integrating the local volume-specific reaction heat across the 1D domain, namely

$$q_r = \int_0^L j^{Li}(\phi_s - \phi_e - U)\,\mathrm{d}x \quad (9)$$

The joule heat is given by

$$q_j = \int_0^L \sigma^{eff}\left(\frac{\partial \phi_s}{\partial x}\right)^2 + \kappa^{eff}\left(\frac{\partial \phi_e}{\partial x}\right)^2 + \kappa_D^{eff}\left(\frac{\partial \ln c_e}{\partial x}\right)\left(\frac{\partial \phi_e}{\partial x}\right)\mathrm{d}x \quad (10)$$

which results from the joule heating of ohmic resistances in the solid active materials (the first term on RHS) and the electrolyte (the remaining two terms). An additional joule heat arises from a contact/electronic resistance between current collector and electrodes and is calculated by

$$q_c = I^2 \frac{R_c}{A} \quad (11)$$

The reversible entropic heat, $q_e$, is neglected as a first approximation in the current work due to the lack of the experimental data for this specific Li-ion cell. It has also been shown that this term is usually small as compared with the irreversible heat at high rate discharge [7,9].

To couple the thermal model with the 1D electrochemical model, temperature-dependent physicochemical properties, such as the diffusion coefficient and ionic conductivity of electrolyte, are needed, and the dependence can be generally described by the Arrhenius equation,

$$\Phi = \Phi_{ref} \exp\left[\frac{E_{act,\Phi}}{R}\left(\frac{1}{T_{ref}} - \frac{1}{T}\right)\right] \quad (12)$$

where $\Phi$ is a general variable representing the diffusion coefficient of a species, conductivity of the electrolyte, exchange current density of an electrode reaction, etc., with $E_{act,\Phi}$ denoting the activation energy of the evolution process of $\Phi$, whose magnitude determines the sensitivity of $\Phi$ to temperature.



DOI: 10.1002/er

In the coupled model, the cell temperature is calculated by the thermal energy conservation equation, Equation (8). This temperature is, in turn, fed back to update the electrochemical calculations through temperature-dependent physicochemical properties. Finally the heat generation from the cell is returned to the energy balance equation to update the temperature. The thermal and electrochemical behaviors of a battery are thus fully coupled in our model.

### 3.3. Numerical procedure

A total of five differential equations, Equations (1)–(4) and (8), are solved simultaneously for the five unknowns: $\phi_s$,$\phi_e$,$c_e$, $c_{s,e}(c_{s,e} = c_s|_{r=R_s})$, and $T$. A computational fluid dynamics (CFD) technique is used to solve these equations except for the solid-phase charge conservation equation, Equation (4), which is solved by a finite element discretization based on five unevenly spaced elements, following the reference [8]. This method for microscopic solid-state diffusion provides sufficient resolution for HEV battery simulations.

## 4. RESULTS AND DISCUSSION

Cell voltage is determined by

$$V = \phi_s|_{x=L} - \phi_s|_{x=0} - \frac{R_c}{A} I \tag{13}$$

where $R_c$ lumps all the contact and electronic resistances between the current collector and electrode as well as the impedance of SEI layers. All the parameters used in this study are listed in Table II. These parameters are either directly measured or best estimates based on the information available.

Table II. Model parameters.

| Parameter | Negative electrode | Separator | Positive electrode |
|---|---|---|---|
| Thickness, $L$ (cm) | $40 \times 10^{-4}$ | $25 \times 10^{-4}$ | $35 \times 10^{-4}$ |
| Particle radius, $r$ (cm) | $5 \times 10^{-4}$ | N/A | $5 \times 10^{-4}$ |
| Porosity, $\varepsilon$ | 0.59 | 0.42 | 0.54 |
| Maximum $Li^+$ concentration in solid, $c_{s\,max}$, mol/cm$^3$ | 0.0309 | N/A | 0.0495 |
| Initial electrolyte concentration, $c_e$ (mol/cm$^3$) | $1.2 \times 10^{-3}$ | $1.2 \times 10^{-3}$ | $1.2 \times 10^{-3}$ |
| Exchange current density, $i_0$ (A/cm$^2$) [8] | $3.6 \times 10^{-3}$ | N/A | $2.6 \times 10^{-3}$ |
| Charge-transfer coefficients, $\alpha_a$, $\alpha_c$, [8] | 0.5, 0.5 | N/A | 0.5, 0.5 |
| SEI layer film resistance, $R_{SEI}$ ($\Omega$ cm$^2$) | 0 | N/A | 0 |
| Li diffusion coefficient in solid, $D_s$ (cm$^2$/s) | $2.55 \times 10^{-10}(1.5-x)^{3.5}$ where $x$ = SOC | | $2.0 \times 10^{-10}$ |
| Electrolyte phase Li diffusion coefficient, $D_e$ (cm$^2$/s) [8] | $1.5 \times 10^{-6}$ | $1.5 \times 10^{-6}$ | $1.5 \times 10^{-6}$ |
| Bruggeman tortuosity exponent, $p$ [8] | 1.5 | 1.5 | 1.5 |
| Solid phase conductivity, $\sigma$ (S/cm), [8] | 1.0 | | 0.1 |
| Current collector contact resistance, $R_c$, ($\Omega$ cm$^2$), estimated | 5 | N/A | 10 |
| Activation energy for exchange current density, $E_{act}^{i_0}$ (J/mol), estimated | 30 000 | N/A | 30 000 |
| Activation energy for solid phase Li diffusion coefficient, $E_{act}^{D_s}$ (J/mol), estimated | 50 000 | N/A | 25 000 |
| Activation energy for electrolyte phase Li diffusion coefficient, $E_{act}^{D_e}$ (J/mol), estimated | 10 000 | 10 000 | 10 000 |
| Activation energy for ionic conductivity of electrolyte solution, $E_{act}^{\kappa}$ (J/mol), estimated | 20 000 | 20 000 | 20 000 |
| Electrode plate area, $A$ (cm$^2$) | 970 | | |
| Heat transfer coefficient, $h$ (W/cm$^2$ K), estimated | 20 | | |
| Reference temperature (K) | 298.15 | | |



DOI: 10.1002/er

The model is first validated by constant current charge and discharge experiments at current rates ranging from 1C (1.2 A) to 10C (12 A), at room temperature (25°C). The cell is charged with constant current until the voltage reaches 4.2 V and then is kept at this voltage until the current drops to the cut-off value of 0.1 A. The cell then is discharged with constant current until the voltage drops to 2.8 V. A model–experimental comparison is shown in Figure 3 for the full cell, where it is seen the predictions match the experimental data quite well for a wide range of C-rates. In Figure 3, only the constant current charge portions (without the later stage constant voltage charging) are shown. At low charge/discharge rates, the cell potential stays close to the cell's OCP. As the charge/discharge rate increases, the cell voltage deviates significantly from the OCP due to ohmic (electrolyte ionic resistance), activation (Li insertion/extraction kinetics), and mass transport (Li transport in electrolyte and active material particles) losses.

The measured and predicted cell temperatures are compared in Figure 4 for 1C, 2C, 5C, and 10C charge and discharge cases. There is almost no temperature rise for the 1C case as the generated heat is small and can be readily dissipated to the ambient (fixed at 25°C). As the C rate increases, the cell temperature starts to rise significantly above the ambient temperature. For the 2C charge/discharge cases, the cell temperature remains at ~2–3°C above the ambient temperature after about 0.2 A h charge/discharge capacity when the heat generation and dissipation reaches equilibrium. The model prediction generally agrees with the experimental data. For 5C and 10C charge/discharge, there is no thermal equilibrium and the cell temperature keeps rising. For the 10C charge/discharge cases, the cell temperature increases almost linearly as the joule heat from the contact and electronic resistance between the current collector and electrodes dominates heat generation and dissipation. For all the cases, the model captures the cell temperature reasonably well, indicative of the accuracy of the present ECT model.

Next, the behaviors of negative and positive electrodes are separately examined. Figure 5 shows the model–experimental comparison of the potentials of the positive and negative electrodes vs

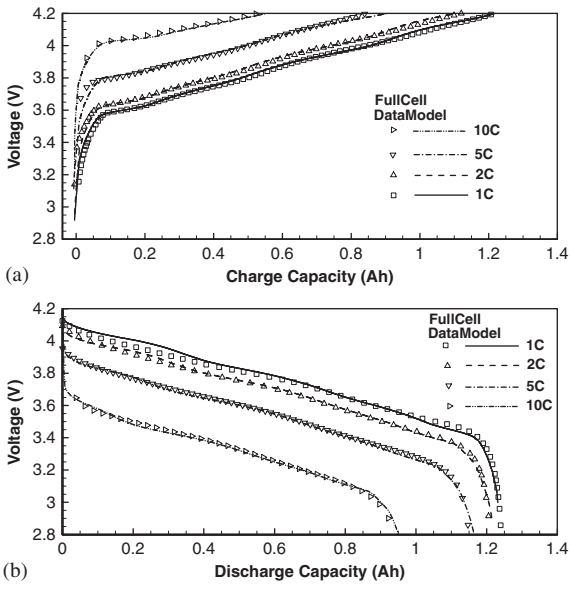


Figure 3. Experimental and simulated of cell voltages for constant current (a) charge and (b) discharge.

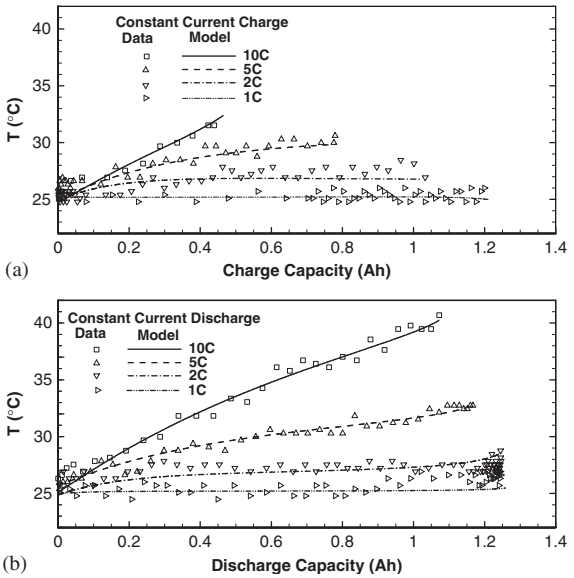


Figure 4. Experimental and simulated cell temperature for constant current (a) charge and (b) discharge. The initial cell temperature and ambient temperature are at 25°C.



DOI: 10.1002/er

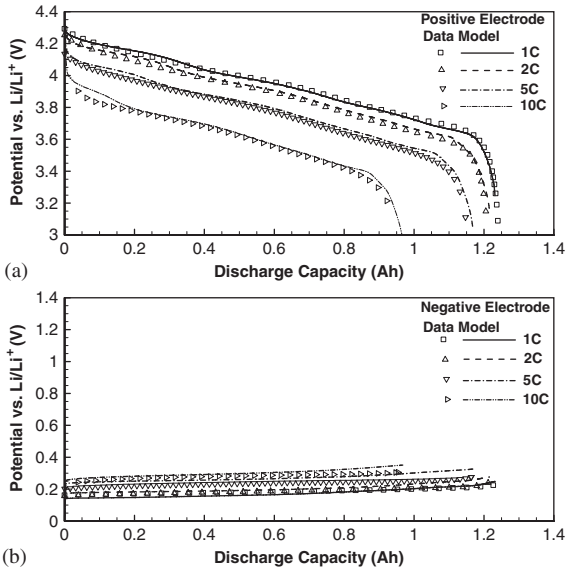


Figure 5. Experimental and simulated (a) positive and (b) negative electrode potential evolutions during constant current discharge.

Li/Li+ during 1C, 2C 5C, and 10C discharge. The overall agreement of individual electrode's potential is seen to be very good. Figure 5(a) shows that the positive electrode potential falls as the discharge current increases from 1C to 10C, while the negative electrode potential rises (Figure 5(b)). As mentioned earlier, this departure from the OCP of each electrode is due to ohmic, kinetic, and mass transport losses. The two plots in Figure 5 also reveal that the effect of high C rate is more substantial on the positive electrode than on the negative electrode.

The model prediction of the local SOC profiles in both negative and positive electrodes during 10C discharge is plotted in Figure 6. Initially, SOC in both electrodes is set at unity. During discharge, SOC values in both electrodes decrease with the SOC of the negative electrode dropping faster than that of the positive electrode in a period between 50 and 100 s. After that, SOC of the positive electrode drops faster and reaches zero earlier, implying that the discharge is stopped due to the limit of the positive electrode. This difference of SOC evolution in the two electrodes can be explained by Figure 7, where the solid-phase Li diffusion coefficients of positive and negative electrodes at 25°C are plotted.

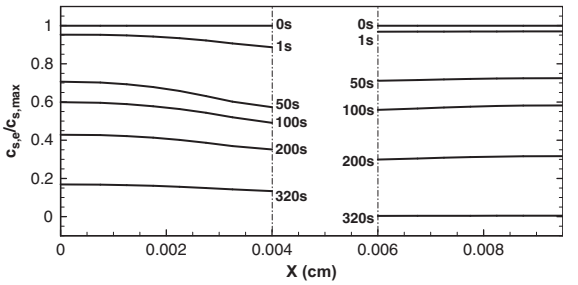


Figure 6. Distribution of the normalized Li concentration at particle surfaces during 10C discharge. The cell regions from left to right are positive electrode, separator, and negative.

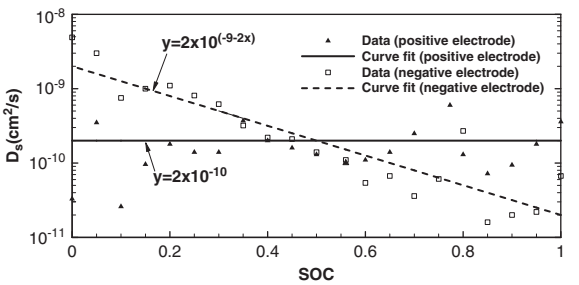


Figure 7. Experimental measurement and curve fit of the solid-phase Li diffusion coefficient in positive and negative electrodes.

The solid-phase Li diffusion coefficient of the positive electrode is measured to be almost constant at $2.0 \times 10^{-10}\,\mathrm{cm}^2/\mathrm{s}$ while its value in the negative electrode is measured to be dependent upon SOC, as shown in Figure 7 [11]. It is seen from Figure 7 that initially the Li diffusivity in the negative electrode is much lower than that of the positive electrode, i.e. $2.25 \times 10^{-11}\,\mathrm{cm}^2/\mathrm{s}$ vs $2.0 \times 10^{-10}\,\mathrm{cm}^2/\mathrm{s}$, such that the SOC of the negative electrode drops faster. However, Li diffusion coefficient in the negative electrode picks up as SOC drops and becomes much higher than that of the positive electrode during the late stage of discharge. This explains why the decreasing speed of SOC in the negative electrode is slower as discharge proceeds. The ability of the ECT model to predict not only overall cell performance, but also internal information such as SOC distributions, is useful for design optimization and in-vehicle control of Li-ion batteries.



DOI: 10.1002/er

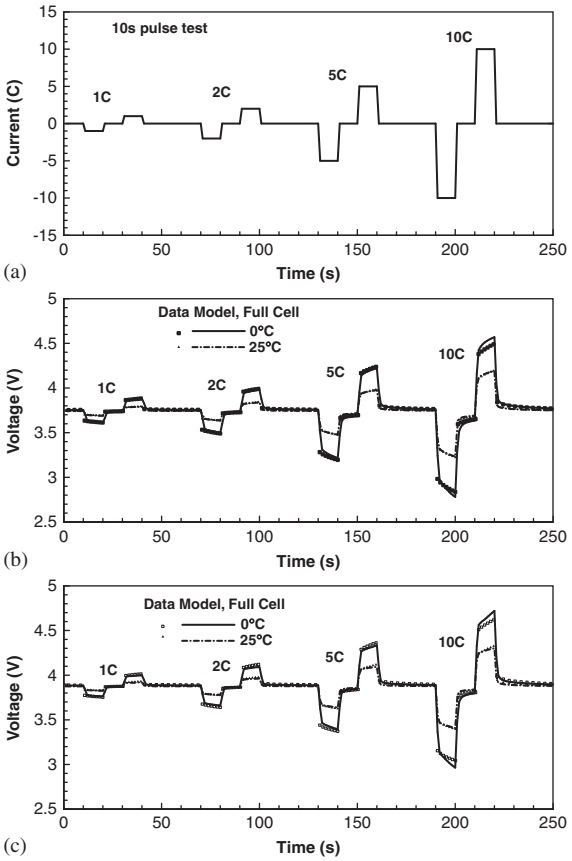


Figure 8. (a) Pulse test current profile, and model validation by experimental data for the cell voltage with initial SOC of (b) 40% and (c) 60% at 25°C and 0°C.

The ECT model's capability of simulating pulse charge/discharge characteristic of HEV application is evident from Figure 8. In this series of tests, 10 s discharge and charge pulses at rates of 1C, 2C, 5C, and 10C are alternated, with open-circuit relaxation in between, as shown in the top plot of Figure 8. These highly dynamic conditions are more challenging for battery simulation as the requirement for temporal resolution is high. Figure 8(b) and (c) shows the simulated and measured results for pulse tests at 25 and 0°C with the initial battery SOC at 40 and 60%, respectively. Again the model prediction closely matches the experimental data. Of particular interest are the pulsing cases at 0°C. While it is widely observed that lithium deposition occurs at high rate, low temperature charging, its fundamental

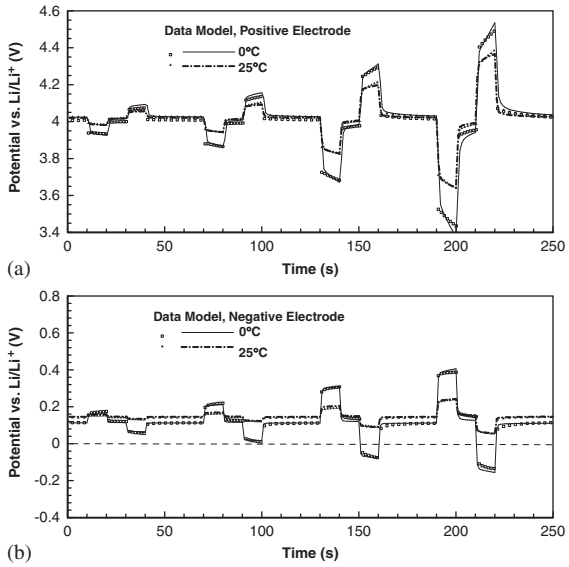


Figure 9. Model validation by experimental data for the potential evolution of (a) positive electrode and (b) negative electrode with initial SOC of 60% at 25°C and 0°C.

mechanism has not been pinpointed clearly. One hypothesis is that the negative electrode potential drops to zero or even negative, thereby thermodynamically favoring Li deposition. Figure 9 thus plots the predicted and measured potential of the negative and positive electrodes separately in these pulsing cases for the initial SOC of 60%. Indeed, it is seen in Figure 9(b) that the negative electrode potential turns negative under 5C and 10C pulse charge, indicating the onset of lithium deposition. Post-mortem material characterization is currently underway to verify whether lithium deposition occurs under these circumstances.

## 5. CONCLUSIONS

An ECT model has been used to explore Li-ion battery performance for HEV application. For the first time, the model was validated against the experimental data for a full cell as well as individual electrodes under constant charge/discharge and pulse conditions representative of HEVs. Good agreement is found between model predictions and experimental measurements obtained using a 3-electrode cell equipped with an



DOI: 10.1002/er

internal thermocouple. The capability of the present ECT model in predicting the negative electrode potential opens the possibility to forecast and prevent the conditions leading to Li deposition and hence capacity loss of automotive Li-ion batteries. Future work includes addition of side reactions to the present performance model so as to capture degradation processes and develop a predictive tool for the battery cycle life under typical driving conditions. Finally, control strategies for mitigating Li-ion battery degradation are to be explored.

## ACKNOWLEDGEMENTS

Financial support of ECEC sponsors for this work is greatly acknowledged.

## REFERENCES

1. Miller T. Advances in NiMH and Li-ion batteries for full hybrids. *Advanced Automotive Batteries Conference*, Baltimore, 2006.
2. Fuller TF, Doyle M, Newman J. Simulation and optimization of the dual lithium ion insertion cell. *Journal of the Electrochemical Society* 1994; **141**:1–10.
3. Doyle M, Fuller TF, Newman J. Modeling of galvanostatic charge and discharge of the lithium/polymer/insertion cell. *Journal of the Electrochemical Society* 1993; **140**:1526–1533.
4. Doyle M, Newman J. Comparison of modeling predictions with experimental data from plastic lithium ion cells. *Journal of the Electrochemical Society* 1996; **143**:1890–1903.
5. Wang CY, Gu WB, Liaw BY. Micro-macroscopic coupled modeling of batteries and fuel cells. Part I: model development. *Journal of the Electrochemical Society* 1998; **145**:3407–3417.
6. Gu WB, Wang CY. Thermal and electrochemical coupled modeling of a lithium-ion cell, in lithium batteries. *ECS Proceedings* 2000; **99–25**:748–762.
7. Srinivasan V, Wang CY. Analysis of electrochemical and thermal behavior of Li-ion cells. *Journal of the Electrochemical Society* 2003; **150**:A98–A106.
8. Smith K, Wang CY. Solid-state diffusion limitations on pulse operation of a lithium-ion cell for hybrid electric vehicles. *Journal of Power Sources* 2006; **161**:628–639.
9. Smith K, Wang CY. Power and thermal characterization of a lithium-ion battery pack for hybrid electric vehicles. *Journal of Power Sources* 2006; **160**:662–673.
10. Zhang Y, Wang CY. Cycle-life characterization of automotive Li-ion batteries with $LiNiO_2$ cathode. *Journal of the Electrochemical Society* 2009; **156**:A527–A535.
11. Kwon OJ, Wang CY. Diagnostics of automotive Li-ion batteries. *Journal of Power Sources* 2009; to be submitted.



DOI: 10.1002/er